

specific absorption rate (SAR) at 3T. The use of FSE makes radiofrequency heating more serious. Compared to SE and FSE, FSPGR provides relatively low radiofrequency heating and, if the NEX of FSPGR can be reduced, relatively short acquisition time. This depends on the signal-to-noise ratio, and we thought it possible based on our rat brain images (Fig. 6). Therefore, we examined the characteristics of signal enhancement in FSPGR. FSPGR provided significantly higher signal enhancement than FSE and comparable signal enhancement to SE, both in the 0.15-mM Gd-DTPA solution and in rat brain C6 glioma in the thalamus region. We speculate that FSPGR may be superior to FSE and comparable to SE in its ability to delineate brain tumors, although, in order to verify this speculation, several studies would be required using different cell types and various transplantation sites. Considering the advantage of FSPGR in terms of acquisition time and SAR limit, FSPGR may be more suitable for contrast-enhanced T1W imaging of brain tumors in clinical 3T scanners than SE. Additionally, high-resolution 3D images can be obtained by using FSPGR with a reasonable acquisition time so that small lesions may be better visualized. On the other hand, FSPGR was more sensitive to magnetic susceptibility artifacts than SE (Fig. 6). SE could therefore be more suitable than FSPGR for delineation of tumors in regions with susceptibility artifacts, such as the base of the skull.

$E_T$  values obtained in our study (1.26 for FSPGR, 1.20 for SE, and 1.12 for FSE) were lower compared to previously reported values (1, 4, 5, 12). For example, RUNGE et al. reported that the  $E_T$  induced by Gd-DTPA was approximately 1.44 using SE in rat brain C6/LacZ glioma models at 3T (5). The difference between  $E_T$  in our study and that in previous reports may result from the difference in the type of tumor, in the degree of growth of brain tumors, or in TR. In our study, TR was adjusted to increase T1 contrast in the normal brain region for specification of more exact location of the glioma. Although the use of a shorter TR may increase signal enhancement in the glioma, contrast in the normal region would become unclear, and therefore it could become difficult to specify the location of the glioma exactly. Therefore, we used a longer TR than that in previous reports.

FISCHBACH et al. showed higher contrast in SE in patients, but they optimized the TR (600 ms) of SE by phantom experiments using a saline solution with a low concentration of Gd-DTPA (0.125  $\mu$ M) (12), whose T1 is extremely long compared to that in the brain. We quantified T1 in rat brains and chose a

proper TR (1400 ms) of SE to enhance normal brain contrast. Therefore, our comparison would be fairer and our results may be more closely extrapolated to human tumors.

One limitation of our work is our limited sample size. Although C6 glioma cells were implanted into 20 rats in our in-vivo study, only five rats could be used for the experiment, as C6 gliomas showed considerable individual variation in their growth and were fully developed only in five rats. Therefore, the number of test animals was relatively small, resulting in large standard deviations for  $E_T$ . A larger sample size may show a significant difference between FSPGR and SE.

In conclusion, FSPGR is superior to FSE and comparable to SE in its ability to delineate rat brain C6 glioma in the thalamus region using venous injection of Gd-DTPA.

#### Acknowledgments

This study was supported by a research grant on Advanced Medical Technology from the Ministry of Health, Labor and Welfare (MHLW), Japan (H17-nano-15), and a Program for Promotion of Fundamental Studies in Health Science of the Organization for Pharmaceutical Safety and Research (of Japan) Health Science Research Grant (H13-005) from the Ministry of Health, Labor and Welfare, (of Japan)

#### References

1. Nöbauer-Huhmann IM, Ba-Ssalamah A, Mlynarik V, Barth M, Schoggl A, Heimberger K, et al. Magnetic resonance imaging contrast enhancement of brain tumors at 3 tesla versus 1.5 tesla. *Invest Radiol* 2002;37:114-9.
2. Trattig S, Ba-Ssalamah A, Nöbauer-Huhmann IM, Barth M, Wolfsberger S, Pinker K, et al. MR contrast agent at high-field MRI (3 Tesla). *Top Magn Reson Imaging* 2003;14:365-75.
3. Ba-Ssalamah A, Nöbauer-Huhmann IM, Pinker K, Schibany N, Prokesh R, Mehraïn S, et al. Effect of contrast dose and field strength in the magnetic resonance detection of brain metastases. *Invest Radiol* 2003;38:415-22.
4. Biswas J, Nelson CB, Runge VM, Wintersperger BJ, Baumann SS, Jackson CB, et al. Brain tumor enhancement in magnetic resonance imaging: comparison of signal-to-noise ratio (SNR) and contrast-to-noise ratio (CNR) at 1.5 versus 3 tesla. *Invest Radiol* 2005;40:792-7.
5. Runge VM, Biswas J, Wintersperger BJ, Baumann SS, Jackson CB, Herborn CU, et al. The efficacy of gadobenate dimeglumine (Gd-BOPTA) at 3 Tesla in brain magnetic resonance imaging: comparison to 1.5

- Tesla and a standard gadolinium chelate using a rat brain tumor model. *Invest Radiol* 2006;41:244-8.
6. Chappell PM, Pele NJ, Foo TK, Glover GH, Haros SP, Enzmann DR. Comparison of lesion enhancement on spin-echo and gradient-echo images. *Am J Neuroradiol* 1994;15:37-44.
  7. Rand S, Maravilla KR, Schmiedl U. Lesion enhancement in radio-frequency spoiled gradient-echo imaging: theory, experimental evaluation, and clinical implications. *Am J Neuroradiol* 1994;15:27-35.
  8. Pui MH, Fok EC. MR imaging of the brain: comparison of gradient-echo and spin-echo pulse sequences. *Am J Roentgenol* 1995;165:959-62.
  9. Fellner F, Holl K, Held P, Fellner C, Schmitt R, Bohm-Jurkovic H. A T1-weighted rapid three-dimensional gradient-echo technique (MP-RAGE) in preoperative MRI of intracranial tumours. *Neuroradiology* 1996;38:199-206.
  10. Li D, Haacke EM, Tarr RW, Venkatesan R, Lin W, Wielopolski P. Magnetic resonance imaging of the brain with gadopentetate dimeglumine-DTPA: comparison of T1-weighted spin-echo and 3D gradient-echo sequences. *J Magn Reson Imaging* 1996;6:415-24.
  11. Elster AD. How much contrast is enough? Dependence of enhancement on field strength and MR pulse sequence. *Eur Radiol* 1997;7 Suppl 5:276-80.
  12. Fischbach F, Bruhn H, Pech M, Neumann F, Ricke J, Felix R, et al. Efficacy of contrast medium use for neuroimaging at 3.0 T: utility of IR-FSE compared to other T1-weighted pulse sequences. *J Comput Assist Tomogr* 2005;29:499-505.
  13. Raula FA, Bowles AP Jr, Perkins E, Terrell A. Sequential imaging and volumetric analysis of an intracerebral C6 glioma by means of a clinical MRI system. *J Neurooncol* 1999;43:11-7.
  14. Thorsen F, Erslund L, Nordli H, Enger PO, Huszthy PC, Lundervold A, et al. Imaging of experimental rat gliomas using a clinical MR scanner. *J Neurooncol* 2003;63:225-31.
  15. Blanchard J, Mathieu D, Patenaude Y, Fortin D. MR-pathological comparison in F98-Fischer glioma model using a human gantry. *Can J Neurol Sci* 2006;33:86-91.
  16. Wansapura JP, Holland SK, Dunn RS, Ball WS Jr. NMR relaxation times in the human brain at 3.0 tesla. *J Magn Reson Imaging* 1999;9:531-8.



## Non-invasive estimation of hepatic blood perfusion from $H_2^{15}O$ PET images using tissue-derived arterial and portal input functions

N. Kudomi · L. Slimani · M. J. Järvisalo · J. Kiss ·  
R. Lautamäki · G. A. Naum · T. Savunen · J. Knuuti ·  
H. Iida · P. Nuutila · P. Iozzo

Received: 30 August 2007 / Accepted: 25 March 2008 / Published online: 6 May 2008  
© Springer-Verlag 2008

### Abstract

**Purpose** The liver is perfused through the portal vein and the hepatic artery. When its perfusion is assessed using positron emission tomography (PET) and  $H_2^{15}O$ -labeled water ( $H_2^{15}O$ ), calculations require a dual blood input function (DIF), i.e., arterial and portal blood activity curves. The former can be generally obtained invasively, but blood withdrawal from the portal vein is not feasible in humans. The aim of the present study was to develop a new technique to estimate quantitative liver perfusion from  $H_2^{15}O$  PET images with a completely non-invasive approach.

**Methods** We studied normal pigs ( $n=14$ ) in which arterial and portal blood tracer concentrations and Doppler ultrasonography flow rates were determined invasively to serve as reference measurements. Our technique consisted of using model DIF to create tissue model function and the latter method to simultaneously fit multiple liver time-activity curves from images. The parameters obtained reproduced the DIF. Simulation studies were performed to examine the magnitude of potential biases in the flow values and to optimize the extraction of multiple tissue curves from the image.

**Results** The simulation showed that the error associated with assumed parameters was <10%, and the optimal number of tissue curves was between 10 and 20. The estimated DIFs were well reproduced against the measured ones. In addition, the calculated liver perfusion values were not different between the methods and showed a tight correlation ( $r=0.90$ ).

**Conclusion** In conclusion, our results demonstrate that DIF can be estimated directly from tissue curves obtained through  $H_2^{15}O$  PET imaging. This suggests the possibility to enable completely non-invasive technique to assess liver perfusion in patho-physiological studies.

N. Kudomi (✉) · L. Slimani · M. J. Järvisalo · R. Lautamäki ·  
G. A. Naum · J. Knuuti · P. Nuutila · P. Iozzo  
Turku PET Centre, University of Turku,  
P.O. Box 52, 20521 Turku, Finland  
e-mail: nobuyuki.kudomi@tyks.fi

J. Kiss · T. Savunen  
Department on Surgery, University of Turku,  
Turku, Finland

H. Iida  
Department of Investigative Radiology,  
Advanced Medical-Engineering Center,  
National Cardiovascular Center-Research Institute,  
5-7-1, Fujishirodai,  
Suita, Osaka 565-8565, Japan

P. Nuutila  
Department of Medicine, University of Turku,  
Turku, Finland

P. Iozzo  
Institute of Clinical Physiology, National Research Council,  
56100 Pisa, Italy

**Keywords** Hepatic blood flow · Input function · Portal vein · Positron emission tomography ·  $H_2^{15}O$

### Introduction

The quantitative determination of hepatic blood flow has the potential to provide important information in the assessment and follow-up of liver disorders, which are almost invariably accompanied by abnormalities in organ

perfusion, representing a prognostic indicator and responding to disease amelioration [4, 10, 19, 21, 28–31, 35]. Positron emission tomography (PET) and  $^{15}\text{O}$ -labeled water ( $\text{H}_2^{15}\text{O}$ ) enable to assess hepatic perfusion quantitatively [29, 30, 35], as based on tracer kinetic modeling, requiring the notion of the time variation of radiotracer concentrations in the liver tissue and in the blood entering the organ (input function).

The liver is characterized by a dual blood supply, comprising the hepatic artery and the portal vein, draining venous blood from the gastrointestinal tract. Thus, in the modeling of PET data from liver, two blood time-activity curves are required to represent the input function (dual input function [DIF]). However, blood withdrawal from a peripheral artery [8, 9, 16, 17, 26, 33] is not always successful and risk-free, and it requires careful correction in time delay between the sampling site and the tissue. More importantly, the portal vein cannot be accessed from any peripheral site, making its blood collection impractical in humans.

The aim of the present study was to develop a new technique to estimate the two components of the DIF non-invasively from dynamic  $\text{H}_2^{15}\text{O}$  PET images. The present

method was characterized by use of a model input function to create a tissue model function, which was used to simultaneously fit multiple tissue curves from PET image. The parameter obtained in the input function model reproduced the input function. Computer simulation studies were performed to examine the magnitude of potential biases in the parameter estimates caused by the inherent assumptions and to optimize the extraction of multiple tissue curves from the image. The present investigation was conducted in pigs because the comparison between measured and estimated values necessitated deep catheterization and invasive Doppler flow measurements.

## Materials and methods

### Theory and computation of non-invasive DIF

A model function was created to shape the input function according to the dose of tracer, administration process, body weight, and physiological state in each subject [18]. The model function introduced is

$$\begin{aligned}
 C_A(t) &= 0. & (t < t_1) \\
 &= \frac{A}{K_1(1+\alpha)} (1 - \exp(K_e(1+\alpha)(t_1 - t))) & (t_1 \leq t \leq t_2) \\
 &= \frac{A}{K_1(1+\alpha)} (\exp(K_e(1+\alpha)(t_1 - t_2)) + \exp(K_e(1+\alpha)(t_2 - t)) - 2 \cdot \exp(K_e(1+\alpha)(t_1 - t))) & (t > t_2)
 \end{aligned} \quad (1)$$

Details of the model function are given in the Appendix. Briefly,  $A$  indicates the height, and  $t_1$  and  $t_2 - t_1$  indicate the appearance time of tracer and administration duration, respectively.  $K_e$  (ml/min) and  $K_1(= \alpha K_e)$  (ml/min) represent the tracer bidirectional diffusion rates between arterial blood and whole body interstitial spaces, respectively.

The portal vein blood model function was generated by introducing the gut compartment model [29–31, 35], that is, a single compartment model between arterial blood and gut compartment, assuming no difference in appearance time between arterial and portal blood (or delay time of portal input), with diffusion rate  $k_g$  in the gut system as

$$C_P(t) = k_g C_A(t) \otimes e^{-k_g t} \quad (2)$$

Using these arterial and portal input model functions, the tissue response function can be expressed by assuming a single tissue compartment model [29–30, 35] and that tracers in arterial and portal blood were well mixed before exchange with liver tissue as

$$C_{\text{TIS}}(t) = (f_a C_A(t) + f_p C_P(t)) \otimes e^{-k_2 t} \quad (3)$$

where  $k_2$  is defined as  $(f_a + f_p)/V_L$ , and  $V_L$  (ml/g) is the distribution volume of water between blood and tissue. In the present study,  $V_L$  was fixed to 0.7 ml/g, which was suggested to fix in a sensitivity analysis by Ziegler et al. [35] and was obtained as  $0.71 \pm 0.03$  ml/g for same subjects in our preliminary evaluation using measured blood input functions. Including a blood volume term into this equation, the model function for liver tracer concentrations, as measured by PET ( $C_{\text{PET}}$ ), can be expressed as

$$\begin{aligned}
 C_{\text{PET}}(t) &= (1 - V_0)(f_a C_A(t) + f_p C_P(t)) \otimes e^{-k_2 t} \\
 &\quad + V_0 C_{\text{input}}(t)
 \end{aligned} \quad (4)$$

where  $C_{\text{input}}(t)$  is defined as

$$C_{\text{input}}(t) = r_a C_A(t) + r_p C_P(t) \quad (5)$$

where  $r_a$  and  $r_p$  are arterial ( $f_a$  ml/min/g) and portal vein blood flow ( $f_p$  ml/min/g) ratios to total hepatic flow, i.e.,  $r_a = f_a/(f_a + f_p)$  and  $r_p = f_p/(f_a + f_p)$  [35]. The flow chart to estimate input functions in this procedure is simplified in



Fig. 1. Multiple tissue time-activity curves (TAC) from liver image were used to estimate the input functions. First, the model function in Eq. 4 was individually fitted to tissue TACs, assuming that  $k_{tr}$  in Eq. 2 is constant by a non-linear fitting method (variable-metric method in the PAW environment: version 2.13/08 [http://www.wasd.web.cern.ch/www/wasd/paw/]), and the set of seven parameters of  $A$ ,  $t_1$ ,  $t_2$ ,  $K_e(1+\alpha)$ ,  $f_a$ ,  $f_p$ , and  $V_0$  in Eqs. 1 and 4 was obtained for each tissue TAC. Then, means and standard deviations of  $t_1$ ,  $t_2$ , and  $r_a (=f_a/(f_a+f_p))$  were calculated, and the tissue TACs with values of  $t_1$  or  $t_2 > 1$  standard deviation of respective means were excluded to avoid the potential influence of TACs outside the liver. In the second step, assuming that all parts of the liver share the same input functions, values of  $t_1$ ,  $t_2$ , and  $r_a$  were fixed to their means,

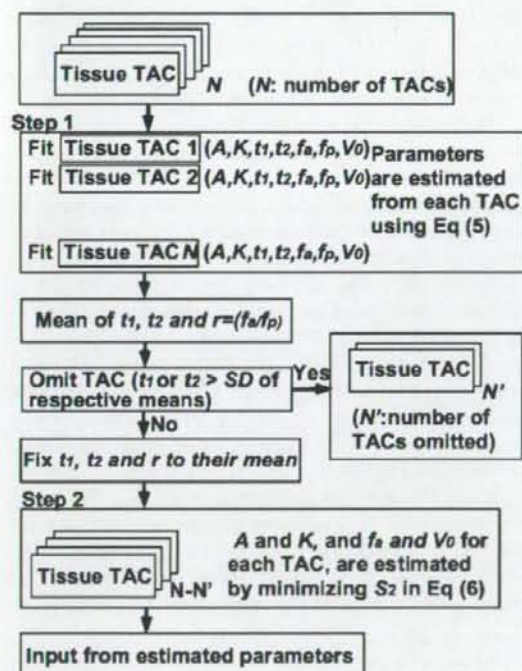


**Fig. 1** A schematic diagram of the procedure to estimate the input functions using multiple tissue TACs. *Step 1* The model function (Eq. 4) was individually fitted to  $N$  tissue time-activity curves (TAC). Then, means and standard deviations of  $t_1$ ,  $t_2$ , and  $r_a$  were calculated, and the tissue TACs with values of  $t_1$  or  $t_2 > 1$  standard deviation of respective means were excluded (indicated as  $N'$  TACs) to avoid the potential influence of TACs outside the liver. In the second step, assuming that all parts of the liver share the same input functions, values of  $t_1$ ,  $t_2$ , and  $r_a$  were fixed to their means, and the other two parameters ( $A$  and  $K_e(1+\alpha)$ ) were estimated by minimizing Eq. 6 by the grid search method. Finally, the image-based input function was obtained by substituting the estimated parameters into Eq. 1

and the other two parameters ( $A$  and  $K_e(1+\alpha)$ ) were estimated by minimizing the following equation:

$$S^2 = \sum_{i=1}^N \sum_{k=1}^K \left( C_{PET}^{i,k} - \left( (1 - V_0') (f_a' C_A(t) + f_p' C_P(t)) \right) \right)^2 \quad (6)$$

$$\odot e^{-k_2 t} + V_0' C_{input}(t)$$

where  $C_{PET}^{i,k}$  is the tissue TAC for  $k$ th frame in  $i$ th tissue region of interest,  $t$  is the corresponding time of  $k$ th frame, and  $f_a'$ ,  $f_p'$  ( $=f_a(1-r_a)/r_a$ ) and  $V_0'$  are values of arterial and portal vein blood flows and of blood volume for  $i$ th tissue, respectively. In this procedure,  $S^2$  was minimized by the grid search method to avoid dependency of initial guess, where  $S^2$  was calculated for 1,000 discrete values of both  $A$  and  $K_e(1+\alpha)$  between ranges of three standard deviations from respective mean values, omitting the negative value. In this procedure, for a given input function, i.e., given  $A$  and  $K_e(1+\alpha)$ ,  $f_a$  and  $V_0$  for each TAC were computed by the grid search method, with acceptable ranges of 0–100 ml/min/g and 0–1 ml/ml, and steps of 1 ml/min/g and 0.01 ml/ml, respectively, and then substituted in Eq. 6. Finally, the image-based input function was obtained by substituting the estimated parameters into Eq. 1.

#### Simulation study

The present method for generating portal vein input assumes that the diffusion rate in the gut system,  $k_{tr}$ , is a fix constant, and there is no time delay between portal and arterial blood. It is not a priori known how these assumed factors degrade the accuracy of estimated DIF and flow. Moreover, tissue TACs from PET images convey some degree of noise, and the accuracy of the estimated input function might depend on either the degree of noise, or the applied number of tissue TACs, or both. A simulation study was designed to reveal the influence of the above elements on the accuracy of the current method.

To this purpose, we selected one arterial curve from one of the present experiments. First, a portal input curve was created by assuming  $k_{tr}=0.5/\text{min}$ , corresponding to the estimated mean in all animals. The combination of these arterial and portal vein curves was treated as the 'true DIF'. In the present experimental study, the average of activity concentrations in an area of the summed image was distributed with a 20% range around the mean for the whole liver, and this percentage was independent of the size of the selected areas in regions  $>50$  pixels. This supports the assumption that flow values in the liver distribute around a 20% range around a mean of arterial flow of 15 ml/min/100 g [22]. Thus, by assuming ten values of  $f_a$  as 13, 13.5, 14, 14.5, 15, 15, 15.5, 16, 16.5, and 17 ml/min/100 g, and ratio  $r (=f_p/f_a)=6$  [22], one set of ten hepatic tissue TACs was generated from the true DIF using Eq. 6.

The propagation of an error in  $k_g$  and delay time to blood flow estimation was simulated. The sequence of steps in this procedure is simplified in Fig. 2a and b. For  $k_g$ , simulated portal input curves were created from the selected

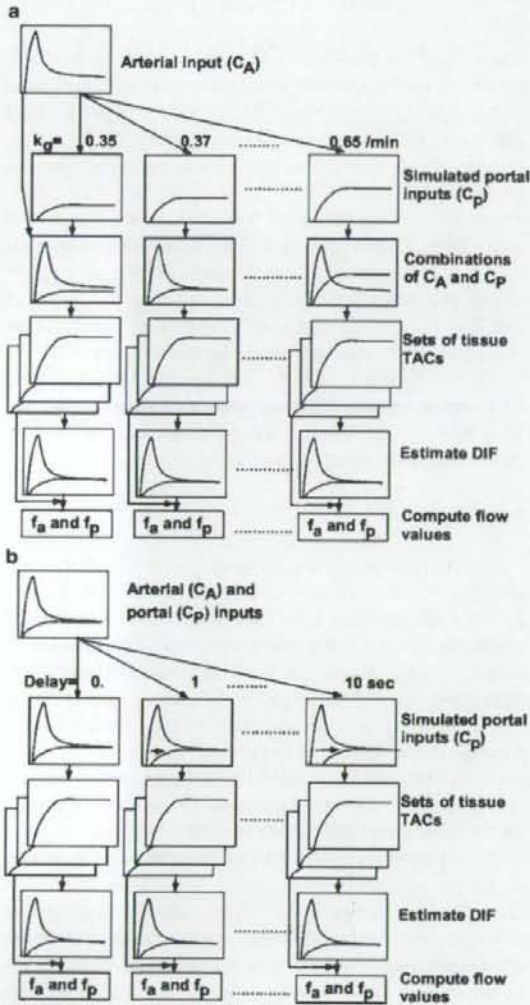


**Fig. 2** Schematic diagram of the procedure to analyze error sensitivity in hepatic arterial ( $f_a$ ) and portal flow ( $f_p$ ) values against assumed  $k_g$  (a) and time delay (b). Portal input curves were created by changing the value of  $k_g$  from 0.35 to 0.65/min in (a) and by shifting the time from 0 to 10 s in (b), respectively, and combinations of the arterial ( $C_A$ ) and simulated portal ( $C_p$ ) curves were used as the simulated dual input functions (DIF). Sets of tissue time-activity curves (TAC) were generated from these simulated DIFs by assuming ten values of  $f_a$  from 13 to 17 ml/min/100 g. In turn, each set of tissue TACs was used to back-estimate DIF fixing  $k_g$  as 0.5/min and time delay as 0.0 s. Finally,  $f_a$  and  $f_p$  were calculated from estimated DIFs for each  $k_g$  and delay time

arterial curve by changing  $k_g$  from 0.35 to 0.65/min for error simulation in  $k_g$ , and combinations of the arterial and simulated portal vein curves were used as the simulated DIF. Sets of tissue TACs were generated from these simulated DIFs, with the same assumptions of  $f_a$  and  $r$  as given above. In turn, each set for each  $k_g$  was used to back-estimate DIF (arterial and portal components), fixing  $k_g$  as 0.5/min in this process as presented above. Finally,  $f_a$  and  $f_p$  were calculated from estimated DIFs for each  $k_g$  by the Gauss-Newton non-linear fitting method in the interactive modeling and data analysis system called PyBLD (<http://homepage2.nifty.com/peco/pybld/pybld.html>) [5] using Eq. 4. For delay time, simulated portal input curves were created from the selected arterial curve by shifting the time from 0 to 10 s, and combinations of the arterial and simulated portal vein curves were used as the simulated DIF. Sets of tissue TACs were generated as above. In turn, each set for each delay time was used to back-estimate DIF fixing time delay as 0.0 s. Finally,  $f_a$  and  $f_p$  were calculated from estimated DIFs for each delay time. Mean of percent difference between computed and assumed ('true') flow values are presented as a function of  $k_g$  and delay time.

The influence of noise versus number of TACs on the accuracy of the method was explored. As shown by Edward et al. [7], as the noise on tissue TACs increased, the standard deviation of uptake ratio of tracer increased; as more regions were used, the standard deviation tended to decrease. However, if the number of TACs is larger, the noise on tissue is also large and vice versa. Our simulation was intended to reveal an optimal number of tissue TACs to be extracted from the whole region of the liver. The procedure is summarized in Fig. 3. First, tissue TACs with noise were generated as follows: Gaussian noise at peak was imposed on the set of ten hepatic tissue TACs generated above. Two levels of noise were introduced, corresponding to 10% and 20% of counts at the level of the peak and 10% and 20% each of the square root of counts at the other points. This procedure was repeated 100 times and 100 sets of noisy tissue TACs, embracing a total of 1,000 pixels obtained. Next, the  $i$ th set of tissue TACs in  $k$ th frame with  $f_a$  defined as  $C_{fa}^{i,k}$  were summed for same  $f_a$  as

$$\bar{C}_{fa}^k = \frac{1}{N_T} \sum_i^{N_T} C_{fa}^{i,k} \quad (7)$$

where  $N_T$  indicates the summed number of tissue TACs and corresponds to the summed number of pixels.  $N_T$  were set to 5, 10, 20, 50, 100, and 200, corresponding to a number of tissue TACs ( $N_{tis}$ ) of 200, 100, 50, 20, 10, and 5, respectively. Here, when  $N_T$  was 200, the 100 tissue TACs were summed as  $N_T=100$  and additionally combinations of  $f_a=13$  and 13.5, 14 and 14.5, 15 and 15, 15.5 and 16, and 16.5 and 17 ml/min/100 g were summed. For each  $N_{tis}$  and



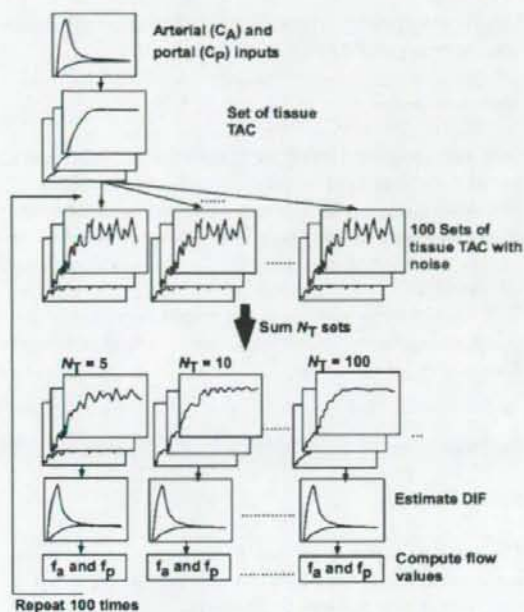


**Fig. 3** Schematic diagram of the procedure to analyze statistical accuracy of hepatic arterial ( $f_a$ ) and portal flow ( $f_p$ ) values against noise on tissue curves. First, tissue time-activity curves (TAC) with noise were generated by imposing Gaussian noise on the set of ten hepatic tissue TACs. This procedure was repeated 100 times, and 100 sets of noisy tissue TACs were obtained. Next, the  $N_T$  (=5, 10, 20, 50, 100, and 200) sets of tissue TACs with the same flow value were summed. For each  $N_T$ , dual input function (DIF) was estimated. Then, arterial ( $f_a$ ) and portal blood flow ( $f_p$ ) values were computed using estimated DIF and tissue TACs. This procedure was repeated 100 times

each level of noise, DIF was estimated, as described. Then, arterial and portal vein blood flow values were computed as above, using estimated DIF and tissue TACs with  $f_a$  of 15 ml/100 g/min. This procedure was repeated 100 times, and the bias and deviation in values of arterial and portal vein flow results were calculated. Their bias and deviation was presented as a function of  $N_{lit}$ .

#### Experimental study

##### PET experiment

Fourteen pigs under anesthesia with weight  $30.0 \pm 1.1$  kg were studied. Data on glucose metabolism in these animals have been previously reported [13, 14]. Animals were deprived of food on the day prior to the study at 5:00 pm. Anesthesia was induced with ketamine (1.0 g) into neck muscles and maintained by ketamine and pancuronium (total of 1.5 g and 40 mg, respectively) administered intravenously during the experiment. Animals were intu-

bated through a tracheostomy, and their respiration was controlled by a ventilator providing oxygen and normal room air (regulated ventilation, 16 breaths per minute). Catheters were inserted into the carotid artery for arterial blood sampling and the femoral vein for administration of  $H_2^{15}O$ . Splanchnic vessels were accessed by sub-costal incision: after dissection of the hepato-gastric ligament, purse string sutures were allocated to allow catheter insertion via a small incision in the portal vein. A catheter was inserted directly in the portal vein for portal vein blood sampling. Ultrasound-based flow-probes (Medi-Stim Butterfly Flowmeter, Medi-Stim AS) were placed around the portal vein and hepatic artery to determine blood velocity in each vessel. The diameter of the hepatic artery and portal vein were measured off-line from B-mode ultrasound images acquired using an Acuson Sequoia 512 mainframe with a 13-MHz B-mode linear array transducer. The area of the vessel was calculated assuming circular shape. Then, blood flow was obtained for each vessel during the PET scans. The surgical access was closed, and the distal catheter extremities were secured to the abdominal surface to avoid tip displacement. The animals were then transported to the PET center for tracer administration, liver imaging, and blood sampling. Vital signs, blood pressure, and heart rate were monitored throughout the study.

PET acquisition was carried out in 2D mode using an ECAT 931-08/12 scanner (CTI Inc, Knoxville, TN, USA) with a 10.5-cm axial field of view and a resolution of 6.7 mm (axial)  $\times$  6.5 mm (in-plane) full width at half maximum. After transmission scan for attenuation correction, the dynamic scan was started after the injection of  $H_2^{15}O$  (274 MBq, 30-s bolus injection), consisting of 20 frames with gradually increasing individual durations ( $6 \times 5$ ,  $6 \times 15$ , and  $8 \times 30$  s).

During PET scanning, blood was withdrawn continuously from the carotid artery and portal vein through catheters (1.4 mm in inner diameter; length of tube was 900 mm to the detector and 60 mm in the detector sensitive region) by using a peristaltic pump (Scanditronix, Uppsala, Sweden) with a withdraw speed of 6 ml/min. Radioactivity concentrations in blood were measured with a BGO coincidence monitor system. The detectors had been cross-calibrated to the PET scanner via ion chamber [26].

At the end of the experimental period, animals were sacrificed by potassium chloride injection and anesthetic overdose, the abdominal cavity was rapidly accessed, and the whole liver was explanted and weighed and its volume was measured by water displacement; liver density was calculated as the ratio of organ weight-to-volume to derive the ultrasound-based flow to PET-equivalent unit (i.e., flow per unit of tissue volume).

The protocol was reviewed and approved by the Ethical Committee for Animal Experiments of the University of Turku.

### Data processing

Dynamic sinogram data were corrected for dead time in each frame in addition to detector normalization. Tomographic images were reconstructed from corrected sinogram data by the median root prior reconstruction algorithm with 150 iterations and Bayesian coefficient of 0.3 [1]. Attenuation correction was applied with transmission data. A reconstructed image had  $128 \times 128 \times 15$  matrix size with a pixel size of  $2.4 \text{ mm} \times 2.4 \text{ mm}$  and  $6.7 \text{ mm}$  with 20 frames.

Measured arterial and portal vein blood TACs were corrected for physical decay and dispersion [11] as  $\tau=2.5 \text{ s}$ , which was experimentally obtained and usually applied in our center. The arterial TAC corrected for decay and dispersion was then corrected for delay by fitting to a whole-liver tissue TAC [12]. The arterial curve obtained,  $C_a(t)$ , was used as the measured arterial input function. Then, the portal vein curve, corrected for dispersion ( $\tau=2.5 \text{ s}$ ) and delay with the same delay time for arterial TAC,  $C_p(t)$ , was fitted according to the following equation:

$$C_p(t) = k_g C_a(t + \Delta t_p) \otimes e^{-k_e(t + \Delta t_p)} \quad (8)$$

to obtain  $k_g$  and to account for the appearance time ( $\Delta t_p$ , seconds) via the gut system. Obtained measured curves were directly fitted with Eqs. 1 and 2 to examine adequacy for a usage of model functions.

A region of interest (ROI) was placed on the whole region of the liver in a summed image and subsequently divided plane-by-plane into sub-regions of 700 pixels each, corresponding to 11–22 sub-regions. Sub-regions were created by extracting pixels firstly from horizontal then vertical directions inside the whole ROI in each slice. Each sub-region consisted of a single area with the same number of pixels. Tissue TACs in the sub-regions were extracted from dynamic images. Then, DIF was estimated according to the procedure introduced above. In the first step, initial values and boundary conditions for the non-linear fitting (PAW environment) for each parameter were 20,000 between 0.0000002 and 200,000,000 Bq/ml for  $A$ , 5 between 2 and 20 ml/min for  $K_d(1+\alpha)$ , 1 between -10 and 100 s for  $t_1$ , 20 between 1 to 60 s for  $t_2-t_1$ , 20 between 1 and 100 ml/min/g for  $f_a$ , 100 between 1 and 400 ml/min/g for  $f_b$ , and 0.05 between 0 and 1 ml/ml for  $V_0$ . In the second step,  $S^2$  value in Eq. 6 was minimized, and the image-based input function was obtained. Areas under the curves (AUC) for measured and image-based inputs were calculated for 0 to 180 s. Their percent difference was calculated.

Perfusion values  $f_a$  and  $f_p$  were calculated by non-linear Gauss-Newton fitting method (PyBLD environment). Results obtained with the new technique were compared with (a) those obtained with the measured input function and (b) the ones from our independent reference method,

i.e., ultrasonography, after their normalization to the organ volume to derive PET-equivalent units.

### Statistical analysis

Data are shown individually or as mean  $\pm$  SD. The Student's paired  $t$  test was used for intra-individual comparisons of flow values. Regression analyses were performed according to standard techniques. A  $p < 0.05$  was considered to be significant. Differences between the flow values were calculated as  $(f_x - f_y)/f_y$ , where  $f_x$  and  $f_y$  are flow values from the non-invasive method and from the measured input or ultrasonography, respectively, and plotted in Bland-Altman plot [3].

## Results

### Simulation study

The biases in values of arterial, portal vein, and total blood perfusion due to a fixed  $k_g$  and delay time are presented in Fig. 4a and b as a function of the value of  $k_g$  and delay time, respectively. The error in total flow results did not exceed 10% for a  $\leq 20\%$  (i.e.,  $0.4\text{--}0.6 \text{ min}^{-1}$ ) difference between the fixed and the assumed (true)  $k_g$  and for a  $< 10\text{-s}$  time delay.

The influence of noise and number of tissue TACs, i.e., the bias and deviation on both arterial and portal blood flow values, showed to be minimal for a number of tissue TACs of 10 to 20 at both noise levels (Fig. 5). As shown in Fig. 5, if the number of tissue TACs is increased, noise on each curve for input estimation becomes larger. On the other hand, a smaller number of tissue TAC corresponds to less information from tissue TAC in terms of variation of flow values. This result suggested that the optimal number of tissue TACs to be applied to preserve accuracy is in the above range, which is independent of the two noise levels. Among the five parameter composing the model input functions, the three parameters  $t_1$ ,  $t_2$ , and  $r_a$  were determined with same accuracy, i.e., both the difference and deviation in those values were less than 1 s for  $t_1$  and  $t_2$  and 5% for  $r_a$ , respectively, for the noise level of 10%, independent of the number of tissue TACs. Bias and deviation of the remaining two parameters  $A$  and  $K_d(1+\alpha)$  depended on the number of tissue TACs following the same tendency as the bias and deviation on blood flow values, as described above.

### Experimental study

Reconstructed images are shown in Fig. 6, together with divided sub-regions. In the first step of our procedure, the



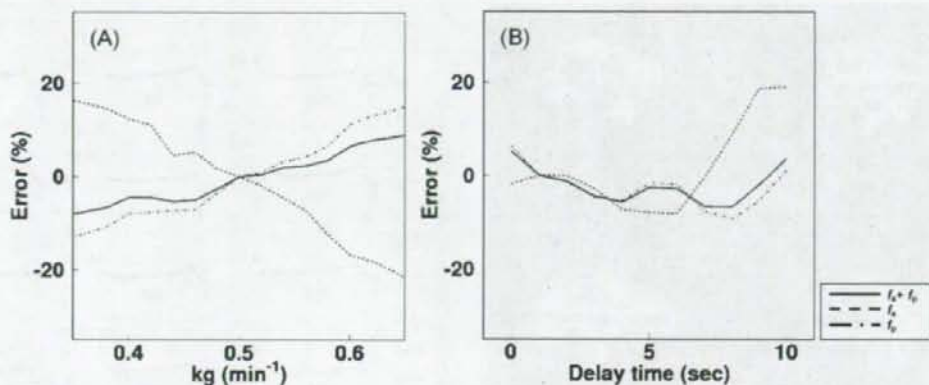


Fig. 4 Error in values of arterial ( $f_a$ ), portal vein ( $f_p$ ), and total ( $f_a+f_p$ ) blood flow propagated from error in  $k_g$  (a) and delay time (b)

obtained value of  $t_1$  from TACs extracted from sub-regions overlapping the vena cava (e.g., lower sub-region at upper left side image in Fig. 6) was 10 to 13 s earlier than the mean, and these TACs were omitted from further processing. The estimated  $t_2-t_1$  was  $27\pm 3$  s, which was similar to the tracer administration duration.

Figure 7 shows the curves of the model arterial and portal input functions (Eqs. 1 and 2) directly fitted to measured curves. The model functions for those were superimposable to measured curves, although both modeled curves slightly overestimated at the late times. This result suggested that the model function was almost adequate to use for the estimation of input.

The mean $\pm$ SD of  $k_g$  was  $0.497\pm 0.153$  ml/min/g and that of  $\Delta t_p$  was  $0.7\pm 5.1$  s obtained by fitting the portal TAC using arterial TAC by Eq. 8.

Estimated, image-derived arterial and hepatic input functions were almost superimposable to the measured curves (Fig. 8). The mean $\pm$ SD and range of difference of

AUCs were  $-3.15\pm 8.73\%$  ranging from  $-13.5\%$  to  $17.9\%$  and  $1.47\pm 8.87\%$  ranging from  $-13.5\%$  to  $10.2\%$  for arterial and portal input functions, respectively. The coefficient of variation of the estimated flow ratio between artery and portal vein in the first step across sub-regions was  $26\pm 9\%$ . The mean $\pm$ SD of that ratio across subjects was  $0.15\pm 0.07$  and those from ultrasonography was  $0.16\pm 0.06$ , and paired  $t$  test showed no significant difference between them. This suggests supporting the assumption that the ratio between arterial and portal input defined in Eq. 5 relates to the flow values.

The Bland-Altman plot between values of hepatic arterial, portal, and total perfusion, as estimated by using the image-derived versus the measured blood curves, is shown in Fig. 9. This plot demonstrates a small overestimation by image-derived method with a bias of 0.01 and 0.07 ml/min/g for arterial and portal flow, respectively, and that 0.08 ml/min/g for total flow. Respective regression lines were the following:  $y=0.00+1.09x$  ( $r=0.97$ ,  $p<$

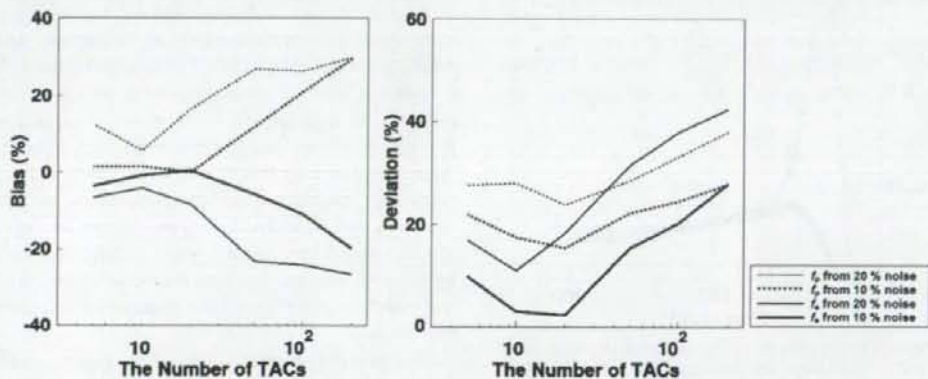
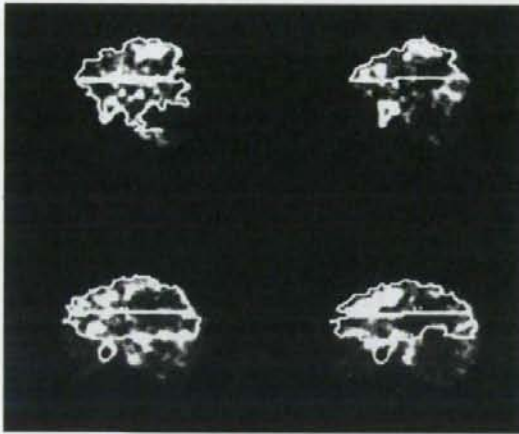


Fig. 5 Bias (left) and deviation (right) in the arterial and portal vein blood flow values as a function of the number of time-activity curves applied to the estimation of the input function



**Fig. 6** View of liver  $H_2^{15}O$  PET images in four slices and sub-regions (solid line). The small area with high activity levels on the mid-right and mid-left side of the image corresponds to the vena cava and aorta, respectively

0.001),  $y=0.05+1.02x$  ( $r=0.87$ ,  $p<0.001$ ), and  $y=0.02+1.06x$  ( $r=0.90$ ,  $p<0.001$ ). Paired  $t$  test showed no significant difference between the methods. Differences were  $-6.8\pm 20.0\%$ ,  $-4.9\pm 14.3\%$ , and  $-5.8\pm 15.6\%$  for arterial, portal, and total blood flow values, respectively.

The Bland–Altman plot between values of hepatic arterial, portal, and total perfusion, as estimated by using the current method versus ultrasonography, is given in Fig. 10. This plot demonstrates an overestimation by image-derived method with a bias of 0.02 and 0.22 ml/min/g for arterial and portal flow, respectively, and that 0.24 ml/min/g for total flow. Respective regression lines were the following:  $y=0.06+0.69x$  ( $r=0.69$ ,  $p=0.12$ ),  $y=0.41+0.98x$  ( $r=0.54$ ,  $p=0.025$ ), and  $y=0.24+0.97x$  ( $r=$

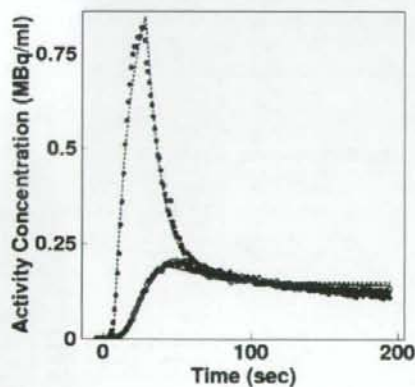


**Fig. 7** Time–activity curves representing the arterial (broken line) and portal (solid line) model input functions (Eqs. 1 and 2) in comparison with the measured arterial (black circles) and portal (open circles) input functions

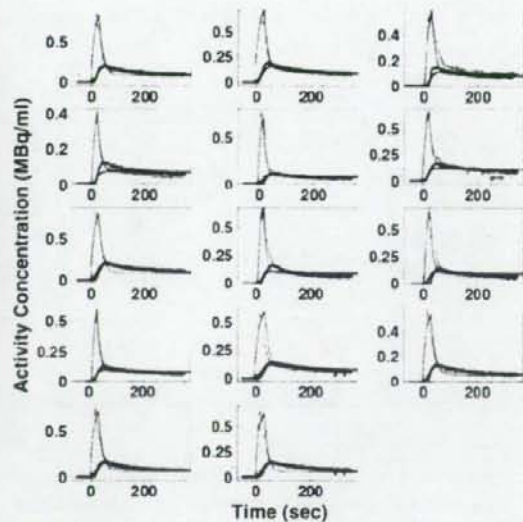


**Fig. 8** Estimated arterial (red line) and portal vein (blue line) input functions from PET images and their comparison with measured arterial (plot in light blue) and portal input (plot in pink) functions

0.60,  $p=0.022$ ). Again, paired  $t$  test showed no significant difference between the methods. Differences were  $3.6\pm 52.0\%$ ,  $15.5\pm 31.3\%$ , and  $16.9\pm 33.0\%$  for values of arterial, portal, and total blood flow, respectively.

The total flow values ranged from 0.5 to 2 ml/min/g in the animals (Figs. 9 and 10). However, only two out of 14 showed smaller values of 0.5 ml/min/g (i.e., approximately 500 ml in the whole organ), which is still physiologically reasonable, while the great majority clustered between 1 and 2 ml/min/g.

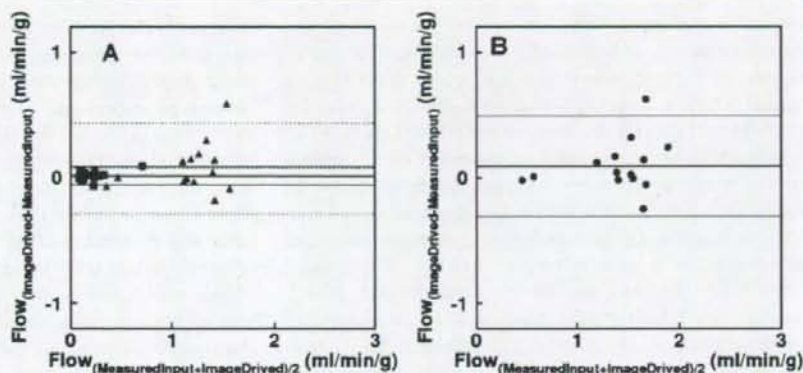
## Discussion

In the current work, we developed and validated a method to estimate the two components of the hepatic dual input function from liver  $H_2^{15}O$  PET images and quantify hepatic perfusion. Computer simulations were used to evaluate the influence of assumptions, noise in raw data, and number and size of the regions of interest to be used in the analysis. After demonstrating that  $k_8$  can be assumed within a 20% range by introducing a negligible error in perfusion estimates and that 10–20 regional time–activity curves appear optimal, the method was validated experimentally by showing its coherence with measured blood tracer levels and with liver perfusion results obtained by an independent technique.

The current approach estimated the hepatic arterial and portal input functions from multiple tissue curves to calculate respective and total organ perfusion. A high



**Fig. 9** **a** Bland–Altman plot for arterial (square), portal (triangle) and **b** total hepatic blood flow differences between measured and image-derived input functions

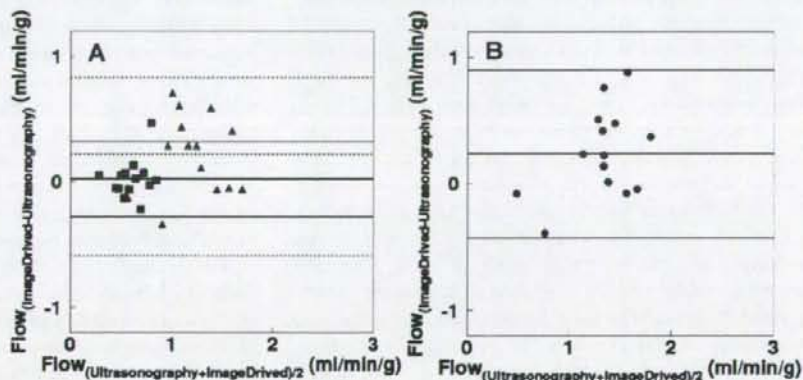


degree of overlap and tight correlations were observed between the estimated input functions and those obtained during online blood sampling/counting. Consequently, calculated flow values were consistent between the methods. Alternative to the present procedure, a ROI-based input extraction from PET images has been used for the carotid artery in [ $^{11}\text{C}$ ]flumazenil brain studies [27], abdominal artery for kidney blood flow quantification with  $\text{H}_2^{15}\text{O}$  [15], and aorta for cardiac  $^{18}\text{F}$ -FDG metabolism [32], and for tumor blood using  $\text{H}_2^{15}\text{O}$  [34]. In these approaches, ROIs are drawn in visible vessels, and the partial volume effect must be taken into account by testing different ROI sizes or by thresholding the pixels inside arterial ROIs; the need for partial volume correction remains a necessary limitation. Closer to the current analysis, Edward et al. applied multiple tissue curves to estimate quantitative kinetic parameters in the brain [7] and well reproduced the input function for  $\text{H}_2^{15}\text{O}$ . However, their formula did not take into account the radioactivity from the blood component inside the tissue ROI, and the validity of their method may not be directly extrapolated to the liver because of the large proportion of blood, which is typically ranging between 0.27 and 0.40 ml/ml [23] in this organ.

The present method showed that the height of the estimated input is almost doubled if the blood volume is not included in the formula and if the arterial volume contributes 10% of radioactivity in the tissue TACs in our preliminary study (data not shown). The shape of an arterial input function from multiple tissue TACs has been well reproduced in brain  $^{18}\text{F}$ FDG or [ $^{11}\text{C}$ ]MPDX studies by using an independent component analysis-based method (extraction of the plasma TAC using independent component analysis [24, 25] still requiring one arterial blood sample, and the combination of the latter and the current techniques may be of further simplification and deserves investigation since it would entail neither a model function nor direct blood measurements.

One advantage of introducing a model function was to shape the model input function by imposing constraints to the parameters range, allowing to overcome noise problems caused by limited scan duration and short half-life of  $^{15}\text{O}$ . The present approach may be applicable to a study group including subjects with hepatic disorders as far as measurement conditions are equivalent and the shape of the input function can be expected to be similar, though the validity of the present method was tested in normal animals. We

**Fig. 10** **a** Bland–Altman plot for arterial (square), portal (triangle), and **b** total hepatic blood flow differences between ultrasonography and kinetic modeling using image-derived input functions



expect no relevant limitation in the extension of the assumptions concerning the shape to other species and in a majority of hepatic conditions. A drawback in the use of a model function, however, is that the feasibility is unknown for a group in which the shape of input functions could be extremely different or cannot be expressed by the present model function. This is not a commonly expected case. In this situation, the present method would require to, and may still be adapted, by introducing group-specific parameter constraints or a modified model function. The present model function was created by assuming the model, namely, tracer bidirectional diffusion to whole body as in differential Eq. 9. The solution was derived as Eq. 10, and the model function was modified to avoid the one order term of  $t$ , which would complicate calculations in the following procedures, i.e., model function for portal input and for tissue response functions. This modification could deteriorate the physiological mean of parameters, such as  $K_e$  and  $K_i$ ; however, the input functions obtained in the present study using this modified equation well reproduced the shape of measured inputs. The modified model function and derived portal model function seemed to be superimposable to measured blood TACs, although there were slight, few-second systematic misalignments in the peak of arterial blood and overestimations at the late phase. This suggested that the error in the position of the peak and in late phase in the estimated input function against measured ones (Figs. 7 and 8) is due to a limitation in the description of the model function.

The present estimation procedure followed two steps, as designed to fit tissue curves individually, and then simultaneously. The first step allowed careful exclusion of tissue TACs showing  $t_1$  or  $t_2$  values over one standard deviation from the mean to eliminate the influence of radioactivity outside the liver region. In fact, in the experimental procedure,  $H_2^{15}O$  was injected in the femoral vein, draining into the vena cava, which is not distant from the liver. Other adjacent high-perfusion organs include the kidneys. The influence of ROIs drawn in proximity of these regions was not included in the model. Thus, special attention was paid at excluding confounding tissue TACs by examining  $t_1$  and  $t_2$ . In the above examples, the tracer was expected to show an early peak in case of an anatomical overlap with the vena cava, and the extracted TAC covering this region was omitted in this step. The second step was introduced to facilitate the achievement of the convergence by fixing the values of  $t_1$ ,  $t_2$ , and  $r_a$  to their calculated means (as obtained above) to estimate the remaining two parameters. Generally, if many parameters are estimated in a fitting procedure such as in the present method, there could be many local minima, and uniqueness of parameter solution might not be guaranteed. As shown in the simulation study, the three parameters  $t_1$ ,  $t_2$ , and  $r_a$  were

estimated independent of the number of tissue TACs; however, the remaining two parameters  $A$  and  $K_e(1+\alpha)$  were dependent on that. This suggests that correlation among parameters due to their numerosity could not be prevented. However, the shapes of input functions were reproduced, and flow values were consistent with other two methods, i.e., those computed from measured inputs and from ultrasonography. Thus, the correlation among parameters did not seem to affect the estimation of flow values, although further study is required for optimization.

We used a fixed value of  $k_g$  to represent the diffusion rate of water between arterial blood and the gut compartment in the estimation of the portal input. The deviation in this rate constant was about 26% in the current study group. The simulation analysis showed that values within 20% of the assumed true  $k_g$  number corresponded to a propagated error of 10% in the final estimation of hepatic perfusion. The value of  $k_g$  used in our final computations is in accordance with the recently reviewed concept that [20] in mammals, the general biological rate (uptake ratio) varies approximately in proportion to the 3/4 power of body size and, given a body mass of ~60 kg,  $k_g$ , which is the uptake rate of water in the gut system, can be predicted to fall around  $0.45 \text{ min}^{-1}$  in humans. This number is consistent with a mean figure of  $0.5 \text{ min}^{-1}$ , as obtained in this study, suggesting that the present assumption could be implemented to obtain the liver input function in humans. We also assumed a time delay of portal input to be zero against the arterial one. The deviation in this time was about 0.7 s in the current study group. The simulation analysis showed that an error in this value within 10 s corresponded to a propagated error of less than 10% in the final estimation of hepatic perfusion. Of further strength, a close agreement was shown between estimated and measured blood activity curves and estimated and Doppler-determined liver flow results. The larger difference of the latter result against the former result might be due to the model assumptions in flow calculations, as well as in the assumption of circular shape when estimating the area of the arterial and portal vessels by ultrasonography and in the accuracy of ultrasonography data (from multiple measurements of flow data, coefficient of variation was  $13 \pm 5\%$  for portal flow and  $18 \pm 10\%$  for hepatic arterial flow with this study [data not shown]). In this study, the flow values were calculated assuming the dual input, single compartment model [2, 29, 30, 35]. Altogether, the above observations support the use of a fixed  $k_g$  and the current model in the fully non-invasive quantification of liver perfusion.

The validation of the current approach, as obtained in this study, is especially valuable in the liver for multiple reasons. First, the inaccessibility of the portal vein prevents its direct blood sampling in humans. Arterial blood can be obtained [8, 9, 16, 17, 26, 33], but blood counting requires corrections for



dispersion, delay between target organ and sampling device, and cross calibration between PET scanner and radioactivity counter, which are all potential sources of errors, in the same magnitude as that expected with the current method. Second, liver perfusion can be compromised both as consequence and cause of hepatic disease and is considered a prognostic indicator and useful marker during progression or treatment follow-up [6, 22]. Third, the possibility to distinctly quantify portal and arterial perfusion is important because their reciprocal compensation may be masked once only if total hepatic flow is measured.

The present simulation study allowed to establish that the optimal number of tissue TACs for DIF estimation was 10 to 20, independent of the noise levels, among the ones selected in this investigation. As pointed out by Edward et al. [7], as the noise on tissue TACs increased, the standard deviation of uptake ratio of tracer increased. Also, they suggested that the standard deviation tended to decrease when more regions were used. The present study intended to investigate the optimal number of tissue TACs from the whole region of liver. The noise in the liver can be minimized by placing a ROI to cover the whole organ and subsequently dividing it in a number of sub-regions corresponding to 10–20 under the conditions of the current experiments. The present results may depend on the reconstruction method. However, as far as the PET image is calculated quantitatively and the distribution of flow values in the extracted TACs is in the same order of magnitude as the present study, the results of optimization in this study would be applicable because those two conditions were assumed in the present simulation study. We assumed that the ratio of blood flow between the hepatic artery and the portal vein was uniform in the whole organ, as supported by an extended literature on the healthy liver and on a majority of metabolic disorders involving the organ. Conversely, the quantification of flow in hepatic tumors in which perfusion from arterial blood is predominant may be best approximated by simplifying the procedure to a single input or by fitting the relative vascular (arterial and portal) contributions as additional parameters in the model. The current procedure was validated for the determination of liver perfusion with  $H_2^{15}O$  PET data. Required conditions were a model function to describe the input function and a kinetic model for tracer exchange between blood and tissue. In theory, the present method might be adapted to other tracers and organs if tracer kinetics in the tissue can be described with a model function.

In conclusion, our results demonstrate that arterial and portal vein concentrations of labeled water can be estimated directly from tissue time-activity curves obtained through dynamic  $H_2^{15}O$  PET imaging. The calculated hepatic arterial, portal, and total perfusion values using estimated or measured input functions were similar and consistent with ultrasonography measurements.

**Acknowledgments** The authors thank the technical staff of the Turku PET Centre for the efforts and skills dedicated to this project. This work is part of the project Hepatic and Adipose Tissue and Functions in the Metabolic Syndrome (HEPADIP, see <http://www.hepadip.org>), which is supported by the European Commission as an Integrated Project under the 6th Framework Programme (contract LSHMCT-2005-018734). The study was further supported by grants from the Academy of Finland (206359 to P.N.), Finnish Diabetes Foundation (P.I.), EFSD/Elis-Lilly (P.I.), Sigrid Juselius Foundation (N.K. and P.I.), and Novo Nordisk Foundation (P.N.).

## Appendix

A model function for AIF was created by assuming a two-compartment model in which the tracer is administered in a rectangular form and diffuses bi-directionally between arterial and interstitial space in whole body peripheral tissue compartments. Differential equations for the model function ( $C_A(t)$ ) can be expressed as

$$\frac{dC_A(t)}{dt} = \frac{dF}{dt} - K_e C_A(t) + K_i C_{WB}(t) \quad (9)$$

$$\frac{dC_{WB}(t)}{dt} = K_e C_A(t) - K_i C_{WB}(t) \quad (10)$$

$$\frac{dF}{dt} = A \quad (t_1 \leq t \leq t_2) \\ 0 \quad (\text{elsewhere}) \quad (11)$$

where  $t_1$  and  $t_2$  assumes the appearance time of administered tracer, and  $t_2 - t_1$  represents the administration duration;  $A$  corresponds to the given amount of tracer. The equation  $F$  (Eq. 11) represents the bolus administration of tracer in the rectangular form with duration  $t_2 - t_1$ .  $C_{WB}(t)$  is the expected tracer concentration in interstitial spaces in whole body peripheral tissues;  $K_e$  and  $K_i$  are bidirectional tracer diffusion rates between blood and peripheral tissue compartments, respectively. Solving Eq. 10 for  $C_{WB}$  gives

$$C_{WB}(t) = K_e e^{-K_i t} \int_0^t C_A(\tau) e^{K_i \tau} d\tau \quad (12)$$

Sum of Eqs. 9 and 10 is

$$\frac{d(C_A(t) + C_{WB}(t))}{dt} = \frac{dF}{dt} \quad (13)$$

Thus,

$$C_A(t) + C_{WB}(t) = F \\ = 0 \quad (t < t_1) \\ = A(t - t_1) \quad (t_1 \leq t \leq t_2) \\ = A(t_2 - t_1) \quad (t > t_2) \quad (14)$$

Substitution of  $C_{WB}$  from Eq. 12 into 14 after multiplying  $e^{K_i t}$  gives

$$e^{K_i t} C_A(t) + K_c \int_0^t C_A(\tau) e^{K_i \tau} d\tau = e^{K_i t} F \quad (15)$$

Differentiation with respect to  $t$  after arranging gives

$$\frac{dC_A(t)}{dt} = \alpha F + \frac{1}{K_c} \frac{dF}{dt} - K_c(1 + \alpha) C_A(t) \quad (16)$$

$$C_A(t) = 0 \quad (t < t_1) \quad (18)$$

$$= \frac{A}{K_c^2(1 + \alpha)^2} \left( K_c \alpha (1 + \alpha) (t - t_1) + 1 - e^{K_c(1 + \alpha)(t_1 - t)} \right) \quad (t_1 \leq t \leq t_2)$$

$$= \frac{A}{K_c^2(1 + \alpha)^2} \left( K_c \alpha (1 + \alpha) (t_2 - t_1) + e^{K_c(1 + \alpha)(t_2 - t)} - e^{K_c(1 + \alpha)(t_1 - t)} \right) \quad (t > t_2)$$

The first term in the second equation for  $t_1 < t < t_2$ , i.e.,  $K_c \alpha (1 + \alpha) (t_1 - t_2)$ , would complicate further calculations (such as tissue response and portal input); thus, this term was omitted, and the model function (Eq. 18) was modified

$$C_A(t) = 0. \quad (t < t_1)$$

$$= \frac{A}{K_c^2(1 + \alpha)^2} (1 - \exp(K_c(1 + \alpha)(t_1 - t))) \quad (t_1 \leq t \leq t_2)$$

$$= \frac{A}{K_c^2(1 + \alpha)^2} (\exp(K_c(1 + \alpha)(t_1 - t_2)) + \exp(K_c(1 + \alpha)(t_2 - t)) - 2 \cdot \exp(K_c(1 + \alpha)(t_1 - t))) \quad (t > t_2) \quad (19)$$

where  $\alpha = K_f/K_e$ . Thus,

$$C_A(t) = K_c e^{-K_c(1 + \alpha)t} \int_0^t \left( \alpha F + \frac{1}{K_c} \frac{dF}{dt} \right) e^{K_c(1 + \alpha)\tau} d\tau \quad (17)$$

Solving Eq. 17, we obtain

to set the  $C_A$  value as 0 at  $t = t_1$ , as continuous at  $t = t_2$ , and as non-zero value at the equilibrium, i.e., at  $t = \infty$ . Thus, the following equation was derived:

## References

1. Alenius S, Ruotsalainen U. Bayesian image reconstruction for emission tomography based on median root prior. *Eur J Nucl Med.* 1997;24:258–65.
2. Becker GA, Muller-Schauenburg W, Spilker ME, Machulla HJ, Piert M. A priori identifiability of a one-compartment model with two input functions for liver blood flow measurements. *Phys Med Biol.* 2005;50:1393–404.
3. Bland JM, Altman DG. Statistical methods for assessing agreement between two methods of clinical measurement. *Lancet.* 1986;1:307–10.
4. Blomley MJ, Coulden R, Dawson P, et al. Liver perfusion studied with ultrafast CT. *J Comput Assist Tomogr.* 1995;19:424–33.
5. Carson RE. Parameter estimation in positron emission tomography. In: Phelps ME, Mazziotta JC, Schelbert HR, editors. *Positron emission tomography and autoradiography: principles and applications for the brain and heart.* New York, NY: Raven; 1986. p. 347–90.
6. Johnson DJ, Muhlbacher F, Wilmore DW. Measurement of hepatic blood flow. *J Surg Res.* 1985;39:470–81.
7. Edward VR, Di Bella EV, Clackdoyle R, Gullberg GT. Blind estimation of compartmental model parameters. *Phys Med Biol.* 1999;44:765–80.
8. Eriksson L, Holte S, Bohm Chr, Kesselberg M, Hovander B. Automated blood sampling system for positron emission tomography. *IEEE Trans Nucl Sci.* 1988;35:703–7.
9. Eriksson L, Kanno I. Blood sampling devices and measurements. *Med Prog Technol.* 1991;17:249–57.
10. Henderson JM, Gilmore GT, Mackay GJ, Galloway JR, Dodson TF, Kutner MH. Hemodynamics during liver transplantation: the interactions between cardiac output and portal venous and hepatic arterial flows. *Hepatology.* 1992;16:715–8.
11. Iida H, Kanno I, Miura S, Murakami M, Takahashi K, Uemura K. Error analysis of a quantitative cerebral blood flow measurement using  $H_2^{15}O$  autoradiography and positron emission tomography, with respect to the dispersion of the input function. *J Cereb Blood Flow Metab.* 1986;6:536–45.
12. Iida H, Higano S, Tomura N, Shishido F, Kanno I, Miura S, et al. Evaluation of regional differences of tracer appearance time in cerebral tissues using  $[^{15}O]$  water and dynamic positron emission tomography. *J Cereb Blood Flow Metab.* 1988;8: 285–8.
13. Iozzo P, Gastaldelli A, Järvisalo MJ, Kiss J, Borra R, Buzzigoli E, et al. 18F-FDG assessment of glucose disposal and production rates during fasting and insulin stimulation: a validation study. *J Nucl Med.* 2006;47:1016–22.



14. Iozzo P, Järvisalo MJ, Kiss J, Borra R, Naum GA, Viljanen A, et al. Quantification of liver glucose metabolism by positron emission tomography: validation study in pigs. *Gastroenterology*. 2007;132:531–42.
15. Juillard L, Janier M, Fouque D, et al. Renal blood flow measurement by positron emission tomography using  $^{15}\text{O}$ -labeled water. *Kidney Int*. 2000;57:2511–8.
16. Kanno I, Iida H, Miura S, Murakami M, Takahashi K, Sasaki H, et al. A system for cerebral blood flow measurement using an  $\text{H}_2^{15}\text{O}$  autoradiographic method and positron emission tomography. *J Cereb Blood Flow Metab*. 1987;7:143–53.
17. Kudomi N, Choi E, Watabe H, Kim KM, Shidahara M, Ogawa M, et al. Development of a GSO detector assembly for a continuous blood sampling system. *IEEE TNS*. 2003;50:70–3.
18. Kudomi N, Watabe H, Hayashi T, Iida H. Non-invasive estimation of arterial input function for water and oxygen from PET dynamic images. *J Nucl Med*. 2006;47(Supplement 1):361.
19. Leen E, Goldberg JA, Anderson JR, et al. Hepatic perfusion changes in patients with liver metastases: comparison with those patients with cirrhosis. *Gut*. 1993;34:554–7.
20. Lindstedt, Schaeffer. Use of allometry in predicting anatomical and physiological parameters of mammals. *Laboratory Anim*. 2002;36:1–19.
21. Martin-Comin J, Mora J, Figueras J, et al. Calculation of portal contribution to hepatic blood flow with  $^{99\text{m}}\text{Tc}$ -microcolloids. A noninvasive method to diagnose liver graft rejection. *J Nucl Med*. 1988;29:1776–80.
22. Materne R, Van Beers BE, Smith AM, Leconte I, Jamart J, Dehoux JP, et al. Non-invasive quantification of liver perfusion with dynamic computed tomography and a dual-input one-compartmental model. *Clin Sci (Lond)*. 2000;99: 517–25.
23. Munk OL, Bass L, Roelsgaard K, Bender D, Hansen SB, Keiding S. Liver kinetics of glucose analogs measured in pigs by PET: importance of dual-input blood sampling. *Nucl Med*. 2001;42:795–801.
24. Naganawa M, Kimura Y, Nariai T, et al. Omission of serial arterial blood sampling in neuroreceptor imaging with independent component analysis. *NeuroImage*. 2005a;26:885–90.
25. Naganawa M, Kimura Y, Ishii K, Oda K, Ishiwata K, Matani A. Extraction of a plasma time-activity curve from dynamic brain pet images based on independent component analysis. *IEEE Trans on Bio-Med Eng*. 2005b;52:201–10.
26. Ruotsalainen U, Raitakari M, Nuutila P, Oikonen V, Sipilä H, Teräs M, et al. Quantitative blood flow measurement of skeletal muscle using oxygen-15-water and PET. *J Nucl Med*. 1997;38:314–9.
27. Sanabria-Bohorquez SM, Maes A, Dupont P, Bormans G, de Groot T, Coimbra A, et al. Image-derived input function for  $^{[11\text{C}]}$  flumazenil kinetic analysis in human brain. *Mol Img Biol*. 2003;5:72–8.
28. Taniguchi H, Oguro A, Takeuchi K, Miyata K, Takahashi T, Inaba T, et al. Difference in regional hepatic blood flow in liver segments—non-invasive measurement of regional hepatic arterial and portal blood flow in human by positron emission tomography with  $\text{H}_2(15)\text{O}$ . *Ann Nucl Med*. 1993;7:141–5.
29. Taniguchi H, Oguro A, Koyama H, Masuyama M, Takahashi T. Analysis of models for quantification of arterial and portal blood flow in the human liver using PET. *J Comput Assist Tomogr*. 1996a;20:135–44.
30. Taniguchi H, Koyama H, Masuyama M, Takada A, Mugitani T, Tanaka H, et al. Angiotensin-II-induced hypertension chemotherapy: evaluation of hepatic blood flow with oxygen-15 PET. *J Nucl Med*. 1996b;37:1522–3.
31. Taniguchi H, Yamaguchi A, Kunishima S, Koh T, Masuyama M, Koyama H, et al. Using the spleen for time-delay correction of the input function in measuring hepatic blood flow with oxygen-15 water by dynamic PET. *Ann Nucl Med*. 1999;13:215–21.
32. Van der Weerd A, Klein LJ, Boellaard R, Visser CA, Visser FC, Lammertsma AA. Image-derived input functions for determination of MRGLu in cardiac  $^{18}\text{F}$ -FDG PET scans. *J Nucl Med*. 2001;42:1622–9.
33. Votaw JR, Shulman SD. Performance evaluation of the pico-count flow-through detector for use in cerebral blood flow PET studies. *J Nucl Med*. 1998;39:509–15.
34. Watabe H, Channing MA, Riddell C, Jousse F, Libutti SK, Carrasquillo JA, et al. Noninvasive estimation of the aorta input function for measurement of tumor blood flow with. *IEEE Trans Med Imaging*. 2001;20:164–74.
35. Ziegler SI, Haberkorn U, Byrne H, Tong C, Kaja S, Richolt JA, et al. Price P. Measurement of liver blood flow using oxygen-15 labelled water and dynamic positron emission tomography: limitations of model description. *Eur J Nucl Med*. 1996;23:169–77.

## Original Article

## Association of Serum Lipocalin-Type Prostaglandin D Synthase Levels with Subclinical Atherosclerosis in Untreated Asymptomatic Subjects

Yoshikazu MIWA<sup>1,2)</sup>, Hiroshi ODA<sup>3)</sup>, Yasuhiko SHIINA<sup>3)</sup>, Kentaro SHIKATA<sup>2)</sup>, Motoo TSUSHIMA<sup>4)</sup>, Satomi NAKANO<sup>4)</sup>, Taro MARUYAMA<sup>4)</sup>, Shingo KYOTANI<sup>4)</sup>, Naomi EGUCHI<sup>5)</sup>, Yoshihiro URADE<sup>5)</sup>, Fumi TAKAHASHI-YANAGA<sup>1)</sup>, Sachio MORIMOTO<sup>1)</sup>, and Toshiyuki SASAGURI<sup>1)</sup>

Recent studies suggest that lipocalin-type prostaglandin (PG) D synthase (L-PGDS), which converts PGH<sub>2</sub> to PGD<sub>2</sub>, is implicated in the pathogenesis of atherosclerosis. However, clinical evidence for the association between serum L-PGDS levels and atherosclerosis has not been reported. In this study, we measured the serum L-PGDS concentration using sandwich enzyme-linked immunosorbent assay (ELISA) and investigated the association with traditional cardiovascular risk factors and surrogate atherosclerotic indices, such as the maximum score of the intima-media complex thickness of the carotid artery (C-IMT<sub>max</sub>) and the brachial-ankle pulse wave velocity (ba-PWV), in 500 non-treated asymptomatic subjects. The serum concentration of L-PGDS was 0.56±0.01 (mean±SEM, range 0.25–1.27, median 0.54) mg/L. Serum L-PGDS levels increased with age and were higher in men than in women. Serum L-PGDS was higher in subjects with hypertension and increased with increasing numbers of the traditional atherosclerotic risk factors. When the subjects were divided into four groups according to the levels of serum L-PGDS, the age-adjusted values of C-IMT<sub>max</sub> and ba-PWV were significantly increased in subjects with higher serum L-PGDS levels (quartile 3 and quartile 4) compared to those in the lowest quartile (quartile 1), for both genders. Multiple regression analysis including risk factors revealed that serum L-PGDS was an independent determinant for ba-PWV ( $\beta=0.130$ ,  $p<0.001$ ). Serum L-PGDS tended to associate with C-IMT<sub>max</sub> but was not statistically significant ( $\beta=0.084$ ,  $p=0.075$ ). In conclusion, our results suggest that an increase in serum L-PGDS concentration is associated with the progression of atherosclerosis. (*Hypertens Res* 2008; 31: 1931–1939)

**Key Words:** lipocalin-type prostaglandin D synthase, intima-media complex thickness, pulse wave velocity, atherosclerosis, arterial stiffness

From the <sup>1)</sup>Department of Clinical Pharmacology and <sup>2)</sup>Department of Medicine and Clinical Science, Faculty of Medical Sciences, Kyushu University, Fukuoka, Japan; <sup>3)</sup>Central Research Institute, Maruha Corp., Tsukuba, Japan; <sup>4)</sup>Department of Internal Medicine, Keio University School of Medicine, Tokyo, Japan; and <sup>5)</sup>Department of Molecular Behavioral Biology, Osaka Bioscience Institute, Suita, Japan.

This study was supported by grants from the Ministry of Education, Culture, Sports, Science and Technology, and the Kyushu University Interdisciplinary Programs in Education and Projects in Research Development.

Address for Reprints: Yoshikazu Miwa, M.D., Ph.D., Department of Clinical Pharmacology, Graduate School of Medical Sciences, Kyushu University, Fukuoka 812-8582, Japan. E-mail: ymiwa@clipharm.med.kyushu-u.ac.jp

Received January 9, 2008; Accepted in revised form August 22, 2008.



## Introduction

Lipocalin-type prostaglandin (PG) D synthase (L-PGDS) is the enzyme responsible for the biosynthesis of the PGD<sub>2</sub> produced in the arachidonic acid cascade from a common precursor of various prostanoids, PGH<sub>2</sub>. This enzyme has recently been reported to have an association with cardiovascular diseases. L-PGDS is expressed in the vascular wall (1, 2) and is overexpressed in the atherosclerotic intima (1). Exogenous L-PGDS inhibits cell proliferation and migration in vascular smooth muscle cells (3). The decrease in L-PGDS production in plaque macrophages increases the risk of plaque rupture through matrix metalloproteinase-9 activation (4). L-PGDS knockout mice fed a high-fat diabetic diet showed accelerated atherosclerosis (5).

The downstream products of L-PGDS, PGD<sub>2</sub> and its naturally occurring metabolites in the PGJ<sub>2</sub> family, such as PGJ<sub>2</sub>,  $\Delta^{12}$ -PGJ<sub>2</sub> and 15-deoxy- $\Delta^{12,14}$ -prostaglandin J<sub>2</sub> (15d-PGJ<sub>2</sub>), have also been reported to show atheroprotective effects by a variety of mechanisms. PGD<sub>2</sub> inhibits platelet aggregation (6), induces vasodilation (7) and suppresses the mRNA expression of pro-inflammatory cytokines such as inducible nitric oxide and plasminogen activator inhibitor-1 in vascular wall cells (8, 9). Among the PGJ<sub>2</sub> family members, 15d-PGJ<sub>2</sub>, a potent endogenous ligand for peroxisome proliferator-activated receptor- $\gamma$  (PPAR- $\gamma$ ), inhibits inducible nitric oxide synthase expression (10), inflammatory cytokine production (11), and matrix metalloproteinase activity in macrophages (12). The PGJ<sub>2</sub> family also strongly inhibits proliferation and promotes differentiation in vascular smooth muscle cells (13–15).

In addition to these findings, several clinical studies have suggested the usefulness of serum L-PGDS measurement in predicting cardiovascular dysfunction. Serum L-PGDS levels were increased in the coronary circulation in patients with angina pectoris (1) and essential hypertension (16), and were suggested to predict the occurrence of restenosis after coronary angioplasty (17). However, these studies analyzed a relatively small population, and the association between serum L-PGDS and atherosclerosis in asymptomatic subjects has not been well examined yet. Therefore, in the present study, we measured the serum L-PGDS concentration using enzyme-linked immunosorbent assay (ELISA) in untreated asymptomatic subjects and investigated the association with the traditional risk factors of atherosclerosis. We also quantitatively assessed the atherosclerotic changes of the vascular wall using two common methods—the maximum value of the intima-media complex thickness of the carotid artery (C-IMT<sub>max</sub>) and the brachial-ankle pulse wave velocity (ba-PWV)—and examined the associations with the serum L-PGDS level.

## Methods

### Subjects

This study involved 512 untreated asymptomatic subjects who participated in an annual health check program from 2001 to 2003 at Kisei-Town (Ise-City, Mie Prefecture, Japan), conducted by Keio University Ise Hospital. Six subjects with severe diabetes (HbA<sub>1c</sub>  $\geq$  8.0%), 4 subjects with severe hyperlipidemia (total cholesterol  $\geq$  7.8 mmol/L [300 mg/dL] or triglyceride  $\geq$  4.5 mmol/L [400 mg/dL]), and 2 subjects with renal impairment (serum creatinine  $\geq$  115  $\mu$ mol/L [1.3 mg/dL]) were excluded and, consequently, 500 subjects were analyzed. Hypertension was defined as systolic blood pressure (SBP)  $\geq$  140 mmHg and/or diastolic BP (DBP)  $\geq$  90 mmHg. Dyslipidemia was defined as low-density lipoprotein (LDL) cholesterol  $\geq$  3.6 mmol/L (140 mg/dL). Diabetes mellitus was defined as fasting plasma glucose (FPG)  $\geq$  7.0 mmol/L (126 mg/dL). This study was conducted in accordance with the Declaration of Helsinki, and the study protocol was approved by the ethics review committee of the Keio University Ise Hospital. Written informed consent was obtained from all subjects.

### Clinical Parameters

At the physical examination, blood pressure, body mass index (BMI), and hematological and biochemical profiles were determined in the morning after an overnight fast. Serum levels of triglyceride, total cholesterol, high-density lipoprotein (HDL) cholesterol, LDL cholesterol, fasting plasma glucose (FPG), and creatinine were measured using routine laboratory methods.

### Measurement of Serum L-PGDS Concentration

Venous blood was collected in the absence of anticoagulant in the morning after an overnight fast. After centrifuge, the serum was aliquoted and stored at  $-80^{\circ}\text{C}$  prior to use. Serum L-PGDS levels were determined by sandwich ELISA using two monoclonal antibodies, Mab-7F5 and Mab-1B7, as described previously (18). In brief, the samples were incubated at  $30^{\circ}\text{C}$  for 90 min in Maxi Sorp F96 microtiter plates (Nalge Nunc, Roskilde, Denmark) precoated with unlabelled Mab-7F5 (4.4 mg/L) at  $4^{\circ}\text{C}$  overnight. After a wash, the plates were incubated at  $30^{\circ}\text{C}$  with peroxidase-conjugated Mab-1B7 (2.0  $\mu$ g/mL) for 90 min. Thereafter, 2,2'-azino-bis(3-ethylbenzothiazoline)-6-sulfonic acid solution (Boehringer-Mannheim, Mannheim, Germany) was added to each well, and the reaction was stopped by adding 1.5% oxalic acid. The plates were read on a Spectra-Max 250 microplate reader (Molecular Devices, Sunnyvale, USA) at 405–492 nm. All samples were measured in duplicate and the results were averaged. The minimal detectable concentration of this assay system

**Table 1. Clinical Characteristics of the Participants**

	Men (n=158)	Women (n=342)	<i>p</i>
Age, years	61.8	59.6	0.041
Body mass index, kg/m <sup>2</sup>	24.0	23.6	n.s.
Systolic BP, mmHg	133.6	130.8	n.s.
Diastolic BP, mmHg	79.8	76.2	0.003
Total cholesterol, mmol/L	5.48	5.67	0.024
HDL cholesterol, mmol/L	1.49	1.64	<0.001
LDL cholesterol, mmol/L	3.36	3.50	n.s.
Triglyceride, mmol/L	1.37	1.15	<0.001
FPG, mmol/L	5.70	5.16	<0.001
Serum creatinine, μmol/L	63.9	84.4	<0.001
Habitual smoking, %	29.3	8.2	0.046
Obesity, %	32.3	29.8	n.s.
Hypertension, %	37.3	33.9	n.s.
Dyslipidemia, %	39.2	43.9	n.s.
Diabetes, %	7.6	3.2	0.030

Values are the mean or frequency. *p* values refer to unpaired *t*-test for continuous variables and  $\chi^2$  analysis for categorical variables. n.s., not significant; BP, blood pressure; HDL, high-density lipoprotein; LDL, low-density lipoprotein; FPG, fasting plasma glucose.

was 0.03 mg/L, and the intra- and interassay coefficients of variation were 3.2 and 5.7%, respectively.

### Carotid Artery Ultrasonography

Ultrasonography of the common carotid arteries was performed with a high-resolution Duplex scanner (SSA-390A; Toshiba Medical Co., Ltd., Tokyo, Japan) using a probe at a frequency of 7.5 MHz for the B-mode scan. The subjects were investigated in the supine position. The carotid arteries were carefully examined with regard to wall changes from different longitudinal (anterior oblique, lateral, and posterior oblique) and transverse views. Each ultrasound image was recorded on a computer with an on-line digital filing system, and the intima-media complex thickness (IMT) was measured off-line and analyzed. This measurement was performed by two independent sonographers blinded from the clinical data. C-IMT<sub>max</sub> was defined as the maximum value of the IMT in the whole area examined, including plaques in bilateral common carotid arteries. The intra-observer and inter-observer coefficients of variation using 50 subjects were 4.6% and 4.3%, respectively.

### Measurement of the ba-PWV

The oscillometric ba-PWV was automatically measured by AT form (Nihon-Colin AT Co., Komaki, Japan) as described previously (19). In brief, this device records the phonocardiogram, electrocardiogram, volume pulse form and arterial blood pressure at the bilateral brachia and ankles. The level of the ba-PWV was calculated by time-phase analysis between the right brachium and ankle. The intra-observer and inter-observer coefficients of variation using 50 subjects were 2.1

and 2.3%, respectively.

### Statistical Analysis

Data are presented as means, means  $\pm$  SEM or frequency. The values for the serum L-PGDS level were used for regression analysis after logarithm-transformation, since these raw values were not normally distributed when we performed the Shapiro-Wilk test and instead showed a logarithm distribution. To compare the mean values between two groups, the unpaired *t*-test was used for continuous variables and the  $\chi^2$  analysis was used for categorical variables. In a simple regression analysis, Pearson's correlation coefficients were used for continuous variables and Spearman's correlation coefficients for categorical variables. To compare the age-adjusted mean values among groups, analysis of covariance was used. Multivariate-adjusted correlations were analyzed by multiple regression models. In a multivariate-adjusted analysis for the C-IMT<sub>max</sub> and ba-PWV, sex (men: 1 or women: 0), age, habitual smoking (yes: 1 or no: 0), obesity (yes: 1 or no: 0), hypertension (yes: 1 or no: 0), dyslipidemia (yes: 1 or no: 0), diabetes mellitus (yes: 1 or no: 0) and log<sub>10</sub> L-PGDS were entered into the model. The above statistical analyses were performed using the JMP IN, version 5.1.1. J (SAS Institute Inc., Cary, USA). The appropriate cut-off values of serum L-PGDS levels for the atherosclerotic indices in the logistic regression model were calculated by plotting the receiver-operating characteristic (ROC) curve using SAS statistical software (SAS Institute Inc.). We defined significant atherosclerosis as a ba-PWV  $\geq$  14.0 m/s (yes: 1 or no: 0) or a C-IMT<sub>max</sub>  $\geq$  1.0 mm (yes: 1 or no: 0), and the points closest to the upper left-hand corner of the graph were chosen as the cut-off points. *p* < 0.05 was



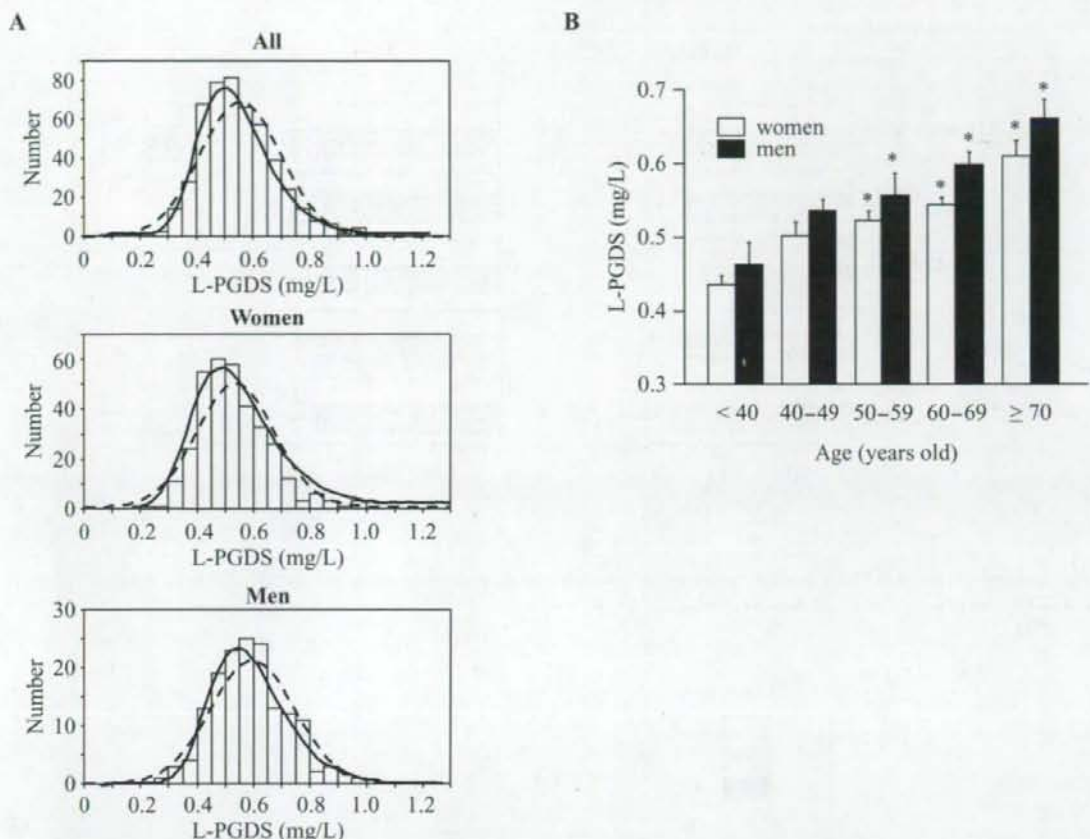


**Fig. 1.** A: Distribution of the serum L-PGDS concentration. The solid and dashed lines represent logarithmic and normal distributions, respectively. B: Serum L-PGDS levels in the indicated age groups. \* $p < 0.05$  vs. <40 years old. L-PGDS, lipocalin-type prostaglandin D synthase.

considered statistically significant.

## Results

### Clinical Characteristics

The characteristics of the participants categorized by sex are presented in Table 1. Ages ranged from 34 to 88 ( $60.3 \pm 0.5$ ) years. Men had higher levels than women of diastolic BP, triglyceride, FPG, and serum creatinine, and lower levels of total cholesterol and HDL cholesterol. The prevalence of atherosclerotic risk factors was 15% for habitual smoking, 31% for obesity, 35% for hypertension, 42% for dyslipidemia and 5% for diabetes. The ratios of habitual smoking and diabetes mellitus were higher in men.

### Serum L-PGDS Level and the Association with Traditional Cardiovascular Risk Factors

The serum level of L-PGDS was  $0.56 \pm 0.01$  mg/L (range 0.25–1.27, median 0.54) and showed a logarithm distribution (Fig. 1A). Serum L-PGDS levels increased with aging; the subjects over 50 years old had significantly higher serum L-PGDS levels than those under 40 years old (Fig. 1B). Furthermore, men (0.60 mg/L) had a significantly greater level of serum L-PGDS than women (0.54 mg/L) ( $p < 0.001$ ). This trend did not change when the subjects were categorized by age (Fig. 1B). In a linear regression analysis, the serum L-PGDS (log scale) was positively correlated with age ( $r = 0.382$ ,  $p < 0.001$ ), SBP ( $r = 0.231$ ,  $p < 0.001$ ), DBP ( $r = 0.142$ ,  $p = 0.001$ ), and serum creatinine ( $r = 0.428$ ,  $p < 0.001$ ) and inversely correlated with HDL cholesterol ( $r = -0.181$ ,  $p < 0.001$ ). These associations did not change

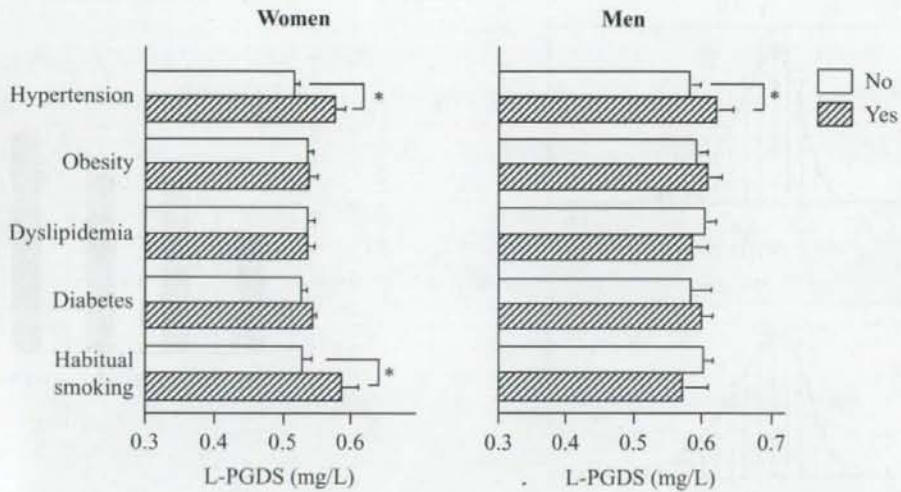


**Fig. 2.** Comparison of L-PGDS levels between subjects with traditional cardiovascular risk factors and those without. \* $p < 0.01$ . L-PGDS, lipocalin-type prostaglandin D synthase.

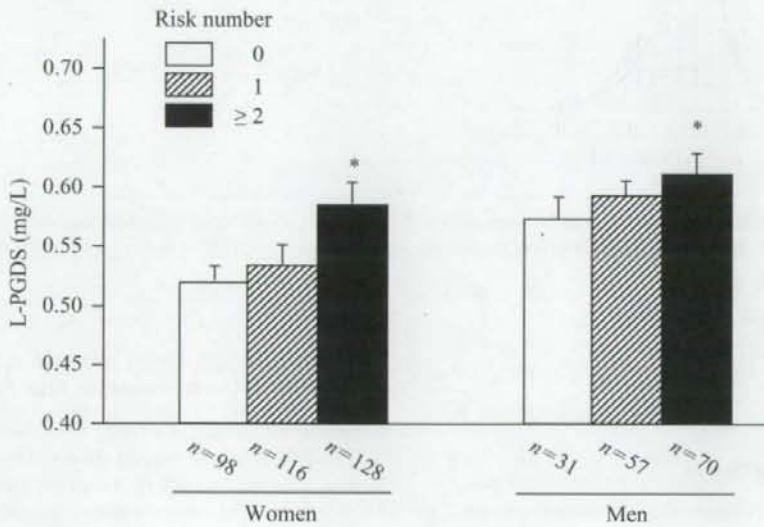


**Fig. 3.** The serum levels of L-PGDS among groups categorized by number of the traditional atherosclerotic risk factors (obesity, habitual smoking, hypertension, dyslipidemia and diabetes). \* $p < 0.05$  vs. the subjects without risk factors (risk number 0). L-PGDS, lipocalin-type prostaglandin D synthase.

when subjects were categorized by gender (data not shown). When the subjects were categorized by the traditional cardiovascular risk factors (habitual smoking, obesity, hypertension, dyslipidemia and diabetes), age-adjusted serum L-PGDS levels were significantly higher in patients with hyper-

tension for both men and women (Fig. 2). In women but not in men, smokers also had higher serum L-PGDS levels than non-smokers. Obesity, dyslipidemia, and diabetes did not show significant differences. However, when the subjects were divided into three groups according to the number of